The role of interface structure in controlling high helium concentrations

Elsevier Editorial System(tm) for Current Opinion in Solid State & Materials Science
Manuscript Draft

Manuscript Number: COSSMS-D-11-00058R1

Title: The role of interface structure in controlling high helium concentrations

Article Type: Review Article

Keywords: helium; helium clusters; helium bubbles; interfaces; grain boundaries; nanocomposites; implantation; mechanical properties; atomistic modeling; transmission electron microscopy

Corresponding Author: Professor Michael J Demkowicz,

Corresponding Author's Institution:

First Author: Michael J Demkowicz

Order of Authors: Michael J Demkowicz; Amit Misra; Alfredo J Caro

Abstract: Interfaces are good traps for implanted He, but are also susceptible to He-induced embrittlement. Better understanding of the mechanisms of He interactions with interfaces may enable design of interfaces that control He while remaining mechanically sound. We review recent work that aims to gain such insight by determining how interface structure influences He trapping and the equation of state of He in interface bubbles as well as how He-induced hardening depends on interface area per unit volume in composite materials.

***Highlights**

Highlights:

- Interfaces may be used to manage He implanted in structural materials
- Misfit dislocations plays a governing role in He interactions with semicoherent interfaces
- Misfit dislocation intersections are trapping sites for He at semicoherent interfaces
- Misfit dislocations modify the equation of state of He stored in a bubble
- He trapping at interfaces influences the mechanical properties of composites

The role of interface structure in controlling high helium concentrations

M. J. Demkowicz[1], A. Misra[2], A. J. Caro[3]

[1]Department of Materials Science and Engineering, MIT, Cambridge MA, 02139
[2]Center for Integrated Nanotechnologies (CINT), Los Alamos National Laboratory, Los Alamos NM, 87544
[3]Structure-Properties Relations Group (MST-8), Los Alamos National Laboratory, Los Alamos NM, 87544

Abstract

Interfaces are good traps for implanted He, but are also susceptible to He-induced embrittlement. Better understanding of the mechanisms of He interactions with interfaces may enable design of interfaces that control He while remaining mechanically sound. We review recent work that aims to gain such insight by determining how interface structure influences He trapping and the equation of state of He in interface bubbles as well as how He-induced hardening depends on interface area per unit volume in composite materials.

Introduction

This paper summarizes the current state of knowledge on helium-interface interactions and describes recent work done by our groups to understand the role of interface structure in controlling and mitigating the deleterious effects of high concentrations of helium. Helium management is of prime concern for materials in future fusion and fast fission reactors [1, 2]. Helium (He)—a seemingly benign element—accelerates swelling by stabilizing void nuclei [3-5] and promotes high-temperature embrittlement by enhancing void growth at grain boundaries (GBs) [6, 7]. In some cases, He-assisted void growth may be so extensive that neighboring voids link up into percolating networks, turning an initially fully-dense metal into a nanoporous solid [8].

Several decades of research have led to a remarkably complex picture of He behavior in metals, spanning multiple length- and time-scales and leaving many open questions [9]. A key discovery made during these years is the "bubble-to-void" transition [10, 11]: under some conditions, a He-filled cavity neither grows nor shrinks, but remains stable as a "He bubble" with diameter less than ~10nm. Under others, it grows without bound by vacancy capture into a "void." Voids are the main culprits in swelling and high temperature embrittlement while bubbles are viewed as comparatively benign or, in some cases, even beneficial [12].

The current engineering approach to He management in structural materials is based on our understanding of the bubble-to-void transition [13, 14] and may be summed up in two imperatives:

1. Maximize the critical radius at which bubbles transform into voids, for example by reducing the concentration of radiation-induced vacancies.
2. Increase the number of stable bubbles by maximizing their number of nucleation sites. This reduces the He flux to individual bubbles for any given He implantation rate.

Both of these guidelines are intended to extend the life of He bubbles and delay their transformation into voids.

One approach to managing He according to these rules is exemplified by nanoferritic alloys (NFAs), such as oxide dispersion-strengthened (ODS) steels. These materials contain a high concentration of nanoscale precipitates that impart strength, recombine radiation-induced point defects, and nucleate He bubbles [15-17]. In this article, however, we will focus on understanding the role of the atomic structure of interfaces in controlling the formation of helium nanoclusters and stable bubbles.

Interfaces with differing crystallographies or compositions may have vastly differing atomic-level structures [18]. Studies of He behavior at interfaces must take this structure into account. In their investigation of He at GBs in austenitic steels, Lane and Goodhew found that He bubble densities were greatest at GBs containing misfit dislocations and that these dislocations were in fact preferred bubble nucleation sites [19]. Singh and his co-workers confirmed the importance of misfit dislocations, but further elaborated that, in aluminum, the preferred bubble nucleation sites are dislocation *intersections*, both within and outside of GBs [20].

In both of these studies, bubble sizes varied from boundary to boundary, but were always larger than in the crystal. This trend was investigated further in high-temperature He implantations in Cu, which showed a correlation between GB energy and He bubble size [21, 22]. The scatter of bubble sizes within a given GB type, however, was large—more than 50%, in some cases—suggesting that other factors besides energy also influence GB-He interactions. Atomistic modeling of He trapping [23, 24], migration [25, 26], and clustering [24, 25] point to the importance of GB structure.

Similar to nanoprecipitates in NFAs, some interfaces may be excellent sites for trapping He in stable bubbles. Many interfaces also impart mechanical strength and recombine radiation-induced point defects [27-30]. Unlike nanoprecipitates, some interfaces are vulnerable to severe embrittlement once He bubbles transform into voids [6, 7]. The range of possible interface structures, however, is vast. Are all interfaces similarly effective in trapping He and similarly susceptible to He-assisted embrittlement? Might it be possible, given control of interface composition and crystallography, to *design* interfaces that both trap He in stable bubbles *and* resist embrittlement?

Studies on the qualitative response to He of isolated interfaces are not sufficient to address these questions. We therefore focus on drawing mechanistic connections between interface structure and interface-He interactions through quantitative investigations of several model interfaces: fcc-bcc heterophase interfaces as well as twist GBs in fcc and bcc metals. All of our model interfaces are semicoherent, i.e. they may be described using misfit dislocation models [18]. Our experiments are centered on magnetron sputtered multilayer nanocomposites because these materials have a high ratio of interface area to total volume. Furthermore, by controlling the thickness of individual layers, this ratio can be varied at will, allowing us to deduce the influence of interfaces on composite properties. Finally, in magnetron sputtered composites, the interfaces between successive layers are all identical, making it easy to connect experiments with atomistic modeling. This review will focus on composites of immiscible metals, though studies on the He-response of miscible metal multilayers have also been carried out [31, 32].

He trapping at fcc-bcc interfaces

He has negligible solubility in crystalline metals [33] and, if introduced in any measurable quantity, rapidly precipitates out in the form of bubbles. It therefore came as a considerable surprise that no He bubbles are detected via transmission electron microscopy (TEM) in some magnetron sputtered Cu-Nb multilayer nanocomposites that were He-implanted to concentrations of more than 5at% [34]. Since similarly He-implanted pure Cu and Nb contain copious bubbles [35, 36], it was inferred that the Cu-Nb interfaces in the composites are responsible for suppressing He bubble formation [35].

To determine what interface-He interactions are responsible for this surprising behavior, an integrated modeling/experimental study was undertaken. Direct evidence for trapping of implanted He was found using neutron reflectometry, which is sensitive to He through its effect on local density. Unlike ion beam analysis techniques, neutron reflectometry has Å-level depth resolution, allowing detection of He at individual interfaces. This techniques was therefore able to demonstrate that regions of high He concentration are localized at Cu-Nb interfaces while bulk Cu and Nb layers remained intact and free of He [37].

At sufficiently high He concentrations, bubbles are eventually resolved via through-focus imaging in TEM at Cu-Nb interfaces [35]. We designed a method for measuring these critical concentrations and demonstrated it on the case of Cu-Nb [38]. In this approach, several multilayers with differing layer thicknesses are synthesized and implanted with He^3. The samples were not annealed, either before or after implantation. The He^3 concentration is then measured as a function of depth by nuclear reaction analysis (NRA), which detects high-energy α particles generated when an implanted He^3 atom fuses with a particle from an incident deuterium beam. We rely on NRA measurements rather than on SRIM [39] because they accurately reflect the true He^3 depth profile, including the effect of any post-implantation

redistribution.

We then compared He^3 depth profiles with bubble distributions found from defocus TEM [38], which can resolve bubbles as small as 1-2nm in diameter [36]. In all samples studied, there was a critical He concentration below which bubbles were not observed, as illustrated in Fig. 1. This concentration scales with interface area per unit volume, as expected when He is preferentially trapped at interfaces. When converted to number of He atoms per unit of *interface area* (rather than sample volume), the critical concentration at which bubbles are observed is the same for all layer thicknesses and equals ~8.5 atoms/nm^2 for Cu-Nb [38]. An analogous study found that the critical interface He concentration in Cu-V multilayers is ~1.9 atoms/nm^2 [40], smaller by nearly a factor of five than in Cu-Nb.

The state of He trapped at interfaces before it takes the form of bubbles detectable in TEM is the topic of an ongoing atomistic modeling effort [41]. Based on the experiments described above alone, we cannot conclude whether or not the critical concentrations we measured correspond to a transition in the way He is stored at these interfaces. Nevertheless, the *relative* difference in critical concentrations measured at different interfaces may already be connected to interface structure using atomistic modeling.

All interfaces in both Cu-Nb and Cu-V magnetron sputtered multilayers form along close packed planes of the neighboring crystals, $\{111\}_{fcc}||\{110\}_{bcc}$, in the Kurdjumov-Sachs orientation relation, where $<110>_{fcc}||<111>_{bcc}$ [42]. We created atomic interface models in agreement with this experimentally determined crystallography [43, 44] and studied their structure and properties using specially constructed EAM potentials to describe interatomic interactions [45]. We found that both interfaces contain two sets of parallel misfit dislocations, illustrated by dashed lines in Fig. 2.a)-d). The intersections between these dislocations form a quasi-periodic pattern within the plane of each interface and play an important role in He trapping.

Figure 2.a) demonstrates the effect of removing an atom (creating a vacancy) near a misfit dislocation intersection (MDI) in the interface Cu plane. The formation energy of the unrelaxed vacancy is 1.5eV, comparable to fcc Cu (1.3eV [46]). Upon annealing for 10ps at 300K followed by energy minimization, the vacancy reconstructs into the configuration in Fig. 2.b) and its formation energy drops to -0.13eV. Thus, the structure in Fig. 2.b) is energetically favorable to the vacancy-free interface and the reconstructed vacancy may be viewed as a constitutional vacancy.

To find ground state interface structures, we iteratively add vacancies until no negative formation energy sites remain. For Cu-Nb, this structure is shown in Fig. 2.c). It has ~25mJ/m^2 lower energy than a vacancy-free interface and contains ~5at% constitutional vacancies concentrated near MDIs, i.e. ~2.5 vacancies per intersection. A similar calculation for a Cu-V interface also shows ~2.5 vacancies per intersection and an energy reduction of ~3.4mJ/m^2. Because the lattice parameters of Nb and V differ, however, the areal density of MDIs in Cu-V is just over a factor of

five smaller than in Cu-Nb, giving an overall ~0.8at% constitutional vacancy concentration, shown in Fig. 2.d).

Due to their constitutional vacancies, MDIs in Cu-Nb and Cu-V contain pockets of excess volume that readily trap He. For example, using a recently-developed Cu-Nb-He potential [41] we found that He interstitial energies at MDIs in Cu-Nb are nearly 2eV lower than in Cu and 1eV lower than in Nb. He substitutional energies are about 0.5eV lower at Cu-Nb MDIs than in Cu and 1eV lower than in Nb. We therefore hypothesize that the difference in critical He concentrations needed to observe bubbles in Cu-Nb and Cu-V arises form differing areal densities of MDIs at these interfaces. Both the critical He concentration per unit interface area and the areal density of MDIs is about five times higher in Cu-Nb interfaces than in Cu-V, in agreement with our deduction.

The areal density of MDIs in any fcc-bcc interface may be computed directly using O-lattice theory [47], allowing us to make mechanistically-informed predictions for the relative He trapping efficiency of all fcc-bcc interfaces. Figure 3 plots computed MDI densities for interfaces formed along close-packed planes in the Kurdjumov-Sachs orientation relation between a number of fcc-bcc element pairs with lattice parameter ratios a_{bcc}/a_{fcc} ranging from 0.7 to 0.95. Also plotted are critical He concentrations per unit interface area obtained on Cu-Nb [38], Cu-V [40], and more recently on Cu-Mo [48]. The agreement between these two sets of data is excellent and predicts that about 25 He atoms may be trapped at a singe MDI before a bubble visible in TEM forms.

To further confirm our hypothesis that He trapping at semicoherent interfaces is governed by MDI density, we investigated interfaces that nominally contain no MDIs. One such interface is the coherent $\Sigma 3$ twin in Cu. In agreement with previous studies [19, 21], no measurable effect of these boundaries on He bubble formation was observed, even in nanotwinned Cu, where the boundary area per unit volume is high [49].

Based on Fig. 3, it appears that Ag-V may also contain no MDIs. Unlike the other fcc-bcc systems we studied, however, magnetron sputtered Ag-V multilayers did not contain just one type of interface. Detailed TEM analysis found that each successive layer in multilayered Ag-V is polycrystalline [50]. Neighboring Ag and V grains have a variety of orientation relations, including Kurdjumov-Sachs, Nishiyama-Wasserman, Bain, Pitsch, and intermediate ones. A range of interface plane orientations were also observed, many of them non-close-packed. Some interfaces were wavy and seemed to contain disconnections [51]. The critical He concentration per unit area in Ag-V represents an average of all observed interface types and therefore does not follow the trend in Fig. 3. Its value is comparable to that of Cu-Nb [52], suggesting a predominance of interfaces with high MDI density.

Hardening due to He bubbles in metallic nanocomposites

If interfaces are to be used to "manage" implanted He, it is crucial to understand the impact that trapped He bubbles or fine He precipitates may have on strength and deformability. A convenient way to study hardening due to He bubbles is to use model systems of fixed geometry such as the nanoscale metallic multilayers discussed in the previous section. In these multilayers, interface structures and spacings may be independently varied, via choice of constituent layers and deposition parameters, respectively.

He is introduced into these materials by ion implantation. Through appropriate choice of implantation conditions, a uniform distribution of He bubbles (~2 nm in diameter) can be produced over 1μm or higher depth [53], making it possible to probe hardness using nanoindentation. Additionally, micropillar compression samples can be machined via focused ion beam milling from the implanted region to perform compression tests and measure stress-strain curves [53]. Figure 4 is a cross-section, under-focused bright field TEM micrograph that shows He bubbles in a Cu-Nb multilayer with a 5nm nominal layer thickness [54].

Before discussing the results of He bubble hardening in multilayers, we review the unit mechanism of dislocation interaction with point obstacles, shown schematically in Fig. 5. The resolved shear stress needed to move a dislocation past two penetrable obstacles a distance *l* apart is

$$\tau = \frac{\mu b}{2\pi l} \ln\left(\frac{l}{r}\right)(\cos\phi_c)^{1/2}, \quad (1)$$

where ϕ_c is half of the critical bow-out angle between dislocation lines cutting through the obstacle (Fig. 5), b is the Burgers vector, μ the shear modulus, and *r* is the obstacle radius [55-58]. When $\phi_c = 0$, Eqn. 1 reduces to the Orowan formula. Recently, Osetsky and Bacon [59] used molecular dynamics to compute ϕ_c for the case of dislocation interactions with voids, thereby making it possible to compute their hardening effect.

In multilayers, in addition to a distribution of bubbles with radius *r* and average spacing *l*, there is also the interphase boundary spacing (i.e. layer thickness), *h*. Thus, both bubbles and layer thickness contribute to hardness (Fig. 6a). However, the flow strength of multilayer materials (in the absence of bubbles) depends on *h* via different unit mechanisms [27, 60-63]: from sub-microns to microns, the Hall-Petch behavior based on dislocation pile-ups dominates; from tens of nanometers to a few hundreds of nanometers, confined layer slip (CLS)-based models dominate; and for thickness of a few nanometers, dislocation crossing of interfaces dominates.

The CLS stress scales directly with $h^{-1}\ln(h/b)$ [27]. When the CLS stress is added to the bubble hardening estimated from Eqn. 1, the calculated strength matches well

with experimental measurements in a number of multilayers such as Cu-Nb and V-Ag [52, 64, 65] for *h* greater than approximately 10nm. To apply Eqn. 1, bubble spacings and radii are obtained from TEM measurements on implanted samples and the critical bow-out angle is taken from the simulations reported in Ref. [59]. The exact relationship between the He/vacancy ratio in a bubble and the critical bow-out angle for bubbles at interfaces remains to be determined via atomistic modeling.

As the layer thickness is reduced from a few hundred nanometers to below 10 nm, the hardening increment due to bubbles, ΔH, decreases. The dependence of ΔH on *h* is found to fit the following phenomenological form: $\Delta H = H_i(1 - l/h)$, $l \quad h$. Here, *l* is an empirical length constant found to be on the order of the bubble spacing in a number of multilayer systems [65] and H_i is a measure of bubble hardening at very large layer thickness or in the limit of single crystal metals. The physical interpretation of this dependence is that when the average bubble spacing is equal to or larger than the layer thickness, bubble hardening is negligible compared to the CLS hardening.

For *h* below approximately 5nm, however, the unit dislocation mechanism of strengthening changes from CLS to interface crossing in multilayers (Fig. 6b). Here, the effect of He bubbles decorating MDIs at the interfaces on the interface barrier stress to slip transmission cannot be neglected. If the bubble hardening is estimated from Eqn. 1, assuming a confined layer slip unit mechanism, it leads to an erroneous estimate of multilayer flow strength [64]. Atomistic modeling of dislocation transmission across interfaces is then required to compute the hardening.

Experimental measurements indicate significant suppression of bubble hardening [53, 64, 65] at *h* below approximately 5nm. In the absence of dislocation pileup-induced stress concentrations, slip transmission is extremely difficult at fcc/bcc interfaces, even in the absence of bubbles [66] and the relative contribution from nanoscale He bubbles at interfaces is expected to be small. The next section of this article shows that the equation of state (and hence pressure) of He bubbles at interfaces may be different from that in the bulk. Thus, the fine bubbles at MDIs at interfaces may interact more weakly with glide dislocations than those in the bulk. This remains an active area of future research to be explored via atomistic modeling.

Finally, the total He concentration also has an effect on hardening. For *h* greater than approximately 10nm, decreasing the implanted He concentration from 7at% to 1at% leads to a significant decrease in hardening due to a reduction in bubble number density (thereby increasing bubble spacing in Eqn. 1). For *h* below approximately 5nm, however, no significant change in hardening was found for He concentrations of 1at% compared to 7at%. This is particularly interesting since 1at% He in 5nm layer thickness Cu-Nb is below the critical concentration of He to detect bubbles, as discussed in the previous section. This implies that interface He clusters too small to be detected in TEM interact, at least to first order, equally effectively with glide dislocations as the relatively larger bubbles.

He bubbles at grain boundaries in pure metals

He trapping and bubble growth is also sensitive to the structure of GBs. Atomistic simulations of He bubbles in metals and ceramics are now able to give quantitative information on such structure-property relations and provide input for rate theory and phase field models [10, 11, 67]. One of the key quantities appearing in such models is the He pressure inside the bubble.

Equilibrium of a bubble with its surroundings is reached when the chemical potential of He or vacancies inside the bubble and outside (within the host metal matrix) are equal. In its simplest form, the chemical potential of He or vacancies in the matrix with a given concentration equals the formation energy of the defect minus temperature, T, times the configurational entropy at that concentration. Meanwhile, the chemical potential of the defect inside a bubble may be approximated by $P \cdot \Omega$, with P the bubble pressure and Ω the defect volume. Pressure then determines the equilibrium concentration of He atoms and/or metal vacancies close to the bubble. This concentration, if different from the value far from the bubble, determines the flux of defects and therefore the bubble growth rate.

In early theories of bubble evolution, a number of approximate equations of state (EOSs) relating P, T, and density of He were used, including ideal gas and hard spheres [11]. In recent phase field simulations of noble gas bubbles in nuclear fuel, better approximations were used [68], including experimentally measured EOSs for He gas [69-71]. Nonetheless, even these improved EOSs ignore metal-He interactions, which are important at the bubble-matrix interface. It is only now, using atomic scale descriptions of the He-metal interaction, that the precise nature of the EOS of He inside a metal matrix may be determined.

We investigated several aspects of this problem that are relevant for the development of an EOS for He in bulk metals, specifically in α-Fe and Cu, and at GBs in them. As a baseline, we first studied He bubbles in bcc Fe, focusing on the differences between the EOS of pure He in its fluid phase, and that of He in the metal [72]. We also studied He bubbles in FeCr alloys, to explore the influence of Cr as a solute and as a precipitate on the He precipitation behavior.

In typical irradiation situations, He atoms arrive at a bubble both by interstitial and substitutional diffusion. The relative importance of these transport mechanisms depends on many factors, such as the He-to-dpa ratio and the bias for interstitial trapping at sinks. In the interstitial He diffusion case, the density in a bubble increases substantially while in the vacancy diffusion case the density change of the bubble is either small or negative as the bubble transforms into a void. Our simulations mimic the former case. In a He-rich and vacancy poor environment, the growth of a He bubble in Fe and Fe-10at% Cr occurs by yielding of the surrounding

metallic matrix (through the emission of an interstitial dislocation loop) to provide extra room for the He, as shown in Fig. 7. Thus, the deformation resistance of the matrix determines the maximum possible He pressures in a bubble.

Other researchers have also conducted atomic-scale computational studies of maximum pressure and growth mechanisms of He bubbles. For example, Schaublin et al. [73] and Lucas et al. [74] studied bubbles at a variety of He densities to estimate the emission energies of self-interstitials, vacancies, and He interstitials. Stewart and co-workers [75] studied the growth mechanism of small He bubbles in Fe under similar conditions as those used here, namely assuming interstitial He diffusing and precipitating onto interstitial He clusters. They conclude that the volume needed for growth is obtained by emission of Fe interstitials. Once numerous interstitials have been emitted, they coalesce to form a nascent dislocation loop. Our simulations are focused on larger bubbles and show emission of fully formed dislocation loops. A recent report [76] addresses the size at which interstitial emission is observed and below which all the stress is accommodated by lattice distortion. We are not aware of any work reporting a transition between single interstitial emission and dislocation loop emission.

Inside the bubble we find a He distribution that reflects the influence of the He-Fe interaction, creating a core-shell-gap structure with the shell and gap dimensions related to the strength of the He-Fe interaction. This structure affects the pressure-density relation such that for small bubbles it departs significantly from the EOS of pure He, as shown in Fig. 8.

Next, we studied He precipitation and bubble growth at 2° {100} twist GBs in Fe. These boundaries contain two sets of parallel screw dislocations that intersect at right angles to each other. Using Metropolis Monte Carlo we find that the preferred sites for precipitation are the screw dislocation junctions. Using molecular dynamics we load the sample with He and find that, similar to the bulk, the preferred mechanism of bubble growth at a He loading rate of 1 He/ps without vacancy trapping is the emission of interstitial dislocation loops. Unlike in bcc Fe, where interstitial loops move away from the bubble, however, those emitted by bubbles at GBs remain attached to the GB dislocation network.

GB He bubbles of all sizes grown under He-rich/vacancy poor conditions never exceed densities of 2 He/vacancy, where the matrix reaches its limit strength and yields, to create room for the growing bubble. Comparison between bcc Fe and twist boundaries, however, shows that the initial bubble pressure in the former is substantially higher (see Figure 8), making bubble formation at twist boundaries more likely [77]. Lower pressures seem to be a consequence of the relative weakness of the matrix around bubbles at GBs, due to the pre-existing screw misfit dislocation network that facilitates the nucleation of interstitial loops.

Finally, we studied He bubbles in fcc Cu low angle {100} twist boundaries [78]. Similar to Fe, in bubbles grown under He-rich/vacancy poor conditions (i.e.

maximum possible He pressure) the He density never exceeds 2 He/vacancy. At this density, the matrix reaches its limit strength and yields, to create room for the growing bubble. The bubble grows by emission of interstitial dislocation loops that decompose into partials. In fcc Cu, these loops leave the bubble, while at the boundary they remain entangled with the pre-existing misfit dislocations, severely distorting them. As in Fe GBs, we find that the pre-existing dislocations help to decrease the pressure at which bubbles grow by reducing the strength of the material. The energies of the GB bubbles are therefore lower than bubbles in fcc Cu.

When modeling gas-filled bubbles, it is often assumed that the "container" can be characterized by just one parameter, the surface energy, which is responsible for creating a surface tension and a resulting pressure, with no further interaction with the gas inside the bubble. In that case, similar to a rubber balloon, the EOS of the gas inside the container is always the same, regardless of the size or structure of the container: for a given He density there is a resulting pressure. For the cases considered here, the situation is more complex. The metal has an interatomic potential that contributes to the EOS of the gas. If the structure of the metal changes, as when the bubble is located at a dislocation intersection, the contribution of the metal-He interactions to the EOS is different from what it would have been in a perfect crystal. The relationship between the structure of the crystal surrounding a bubble and its effect on the EOS of He is a topic of current investigation.

Our modeling results may be compared to recent experiments on He-implanted Au bicrystals containing low angle {100} twist GBs, similar to the ones we studied in Cu [77]. As shown in Fig. 9, both our modeling and the experiments demonstrate a preference for He to precipitate at the nodes of the dislocation network. Moreover, both studies show that the GB is effective at collecting He bubbles from the neighboring crystalline material as bubbles coarsen.

The ensemble of these results allows us to propose EOSs for bubbles in single-crystal metals and at low angle twist GBs. Both EOSs appear to be substantially different from that of pure He. For a given density and for all bubble radii, the pressure is significantly higher than for pure He, reflecting the influence of the He-metal interaction. The EOS constructed for He bubbles at twist GBs shows that the pressure is always less than or equal to the value in bulk, an effect originated in the softening of the lattice arising from the pre-existing misfit dislocation network, which facilitates the plastic deformation needed for bubbles to grow under vacancy-poor conditions. These results suggest that the dislocation networks characteristic of the interface under consideration may be a dominant factor to determine the pressure for a given density. If this hypothesis is confirmed, it may then be possible to construct EOSs related to particular semicoherent interfaces and in this way identify those that are better for trapping He at their junctions.

Discussion

From previous investigations [19, 20] as well as the work described above, it is clear that misfit dislocation structure plays a governing role in He interactions with both semicoherent heterophase interfaces and grain boundaries. Intersections between misfit dislocations are the preferred trapping sites for He and determine how much of it may be stored in such an interface before detectable bubbles form. Misfit dislocation networks influence the interactions of He with the surrounding metal matrix, thereby modifying the equation of state of He stored in a bubble. The partitioning of He between interfaces and perfect crystalline material influences glide dislocation motion and therefore also the mechanisms of deformation in He-implanted composites.

Based on these insights, we may begin to envision new ways for how interfaces may be designed to manage He implanted into structural materials. For example, by controlling the distribution of misfit dislocation intersections in a semicoherent interface, He bubbles or bubble nuclei may be templated with a desired spacing [79]. The spacing may be optimized to achieve desired behavior, e.g. to maximize or minimize He storage or to influence interface mechanical properties. By tailoring the detailed misfit dislocation configuration, including the character of the dislocations, the equation of state of He trapped in interface bubbles may also be tuned.

Many unresolved questions concerning He behavior at interfaces nevertheless remain. How do small He clusters trapped at misfit dislocation intersections grow into visible bubbles? How does the equation of state of He in bubbles at grain boundaries modify the conditions for bubble-to-void transition? What are the detailed mechanisms of glide dislocation interactions with interface He clusters? How does He interaction with incoherent interfaces? And perhaps most importantly: how is He transported through interfaces? Both of the principles for He management given in the introduction to this article have to do with safe storage of He. Might it be possible not only to delay the deleterious effects of He, but also avert them entirely by continually removing it as it is implanted [80, 81]?

Finally, the work presented here illustrates how integrating experimental and modeling studies may yield insights that neither approach can attain by itself. For example, by combining several different experimental techniques (controlled synthesis, He^3 implantation, neutron reflectometry, TEM, and NRA) with atomistic modeling, we were able to gain quantitative insight into He trapping at fcc-bcc interfaces, despite the fact that currently there is no single experimental method that directly detects individual He atoms. We were also able to relate He trapping to interface structure, even though in the interfaces we studied this structure also cannot be directly imaged (the misfit dislocation spacing is too small to be resolved in TEM). Finally, based on our findings, we were able to make predictions for He trapping at interfaces that were not initially investigated, creating opportunities for further experimental validation and for design of materials containing interfaces that mitigate He-induced degradation.

The materials science community is increasingly recognizing the value of conducting experimental investigations that combine multiple capabilities to study individual problems [82]. To derive maximum benefit from such method integration, experimental studies must be hypotheses-driven. This in turn requires a strong modeling and theory "backbone" to propose good hypotheses, identify experimental methods with the highest likelihood of shedding light on these hypotheses, and to interpret the ensuing experimental results. We believe that such integrated studies will give the kind of detailed understanding needed to create structural materials designed for service in a variety of extreme environments, including ones where materials are exposed to He implantation, heavy ion bombardment [83], and other harsh conditions [84].

Acknowledgements

We thank G.R. Odette, M. Nastasi, J. P. Hirth, and R. G. Hoagland for insightful discussions. This work was supported by the Center for Materials in Irradiation and Mechanical Extremes (CMIME), an Energy Frontier Research Center funded by the U. S. Department of Energy, Office of Science, Office of Basic Energy Sciences under award number 2008LANL1026 and by the Los Alamos National Laboratory LDRD program.

Figure captions

Fig. 1: Comparing the TEM micrograph of a He^3-implanted Cu-Nb multilayer (top) and the corresponding He concentration profile measured by NRA (bottom) reveals a critical depth at which no He bubbles are observed (indicated by dashed lines), even though the He concentration is not zero. [38]

Fig. 2: (a) An unrelaxed vacancy on the Cu side of a Cu-Nb interface, and (b) the same vacancy after relaxation. (c) The ground state Cu-Nb interface with ~5at% constitutional vacancies and (d) ground state Cu-V interface with ~0.8at% constitutional vacancies. Atoms colored red have less than 6 nearest neighbors in the interface Cu plane. Dashed lines indicate interface misfit dislocations. [38]

Fig. 3: Black dots are areal densities of MDIs calculated by O-lattice theory for a range of fcc-bcc pairs with differing lattice parameter ratios, but identical interface crystallographies (Kurdjumov-Sachs orientation relation and closest-packed interface planes). Red diamonds are measured values of critical He concentrations required to observe bubbles in TEM. The dashed line is a guide to the eye.

Fig. 4: Under-focused bright field TEM micrograph showing helium bubbles in a Cu-Nb multilayer with a 5 nm nominal layer thickness. [54]

Fig. 5: Schematic illustration of glide dislocation interaction with point obstacles (nm-scale bubbles in this case) of spacing *l*. Here, *h* refers to the thickness of individual layers for multilayers or the total film thickness for pure metal films. Numbers 1-3 show the steps of dislocation movement through a field of bubbles. ϕ_c is the semi-critical angle at which the dislocation breaks away from pinning points. [65]

Fig. 6: Schematic illustration of the bubble hardening mechanisms in multilayers (the circles indicate bubbles). (a) When the layer thickness is a few tens to a few hundreds of nanometers, $h>>l$ and deformation occurs via confined layer slip (CLS). Dislocations gliding in a layer confined by interfaces are pinned by nanometer-scale bubbles resulting in an additive term to the CLS stress. (b) When the layer thickness is only a few nanometers and $h \leq l$, the yield strength is determined by the crossing of single dislocations across interfaces containing a distribution of nanometer-scale He bubbles in the interface plane. [65]

Fig. 7: Pressure versus number of He atoms in a bubble seeded with an initial cavity of 27 vacancies in Fe (red + curve) and in Fe-10at% Cr (green x curve). Snapshots at 0, 27, and 60 He atoms show He atoms in red and distorted Fe atoms in blue. Snapshots at 140, 260, and 375 He atoms show the moment of emission of interstitial dislocation loops. At 260 He atoms, faceting is clearly seen. [72]

Fig. 8: Room temperature pressures for a single bubble in bcc Fe and bubbles at 2° and 6° twist GBs in Fe. The pressure of pure He fluid at the same density as the bcc Fe bubble is given for comparison. [77]

Fig. 9: a) Plan view of a single crystal Au foil implanted with 22.5 keV He to a dose of $5 \cdot 10^{15}$ cm^{-2} at 250C. b) Plan view of a Au bicrystal containing a ~1° {100} twist boundary, He-implanted the same was as the single crystal in a). The square network of screw misfit dislocations is clearly visible. He bubbles (bright dots) decorate the nodes of the network. c) Metropolis MC simulation at a 2° Au {100} twist boundary showing the mist dislocation network in blue and He bubbles at the nodes in red. Atoms at dislocation cores are shown based on a potential energy threshold. [78]

References

[1] H. Ullmaier, Nucl. Fusion, 24 (1984) 1039-1083.
[2] S.J. Zinkle, N.M. Ghoniem, Fusion Engineering and Design, 51-2 (2000) 55-71.
[3] K. Farrell, Radiat. Eff. Defects Solids, 53 (1980) 175-194.
[4] S.J. Zinkle, W.G. Wolfer, G.L. Kulcinski, L.E. Seitzman, Philos. Mag. A-Phys. Condens. Matter Struct. Defect Mech. Prop., 55 (1987) 127-140.
[5] A.J.E. Foreman, B.N. Singh, Radiat. Eff. Defects Solids, 113 (1990) 175-194.

[6] H. Schroeder, W. Kesternich, H. Ullmaier, Nuclear Engineering and Design/Fusion, 2 (1985) 65-95.
[7] D.N. Braski, H. Schroeder, H. Ullmaier, J. Nucl. Mater., 83 (1979) 265-277.
[8] S. Kajita, W. Sakaguchi, N. Ohno, N. Yoshida, T. Saeki, Nucl. Fusion, 49 (2009) 095005.
[9] H. Trinkaus, B.N. Singh, J. Nucl. Mater., 323 (2003) 229-242.
[10] L.K. Mansur, W.A. Coghlan, J. Nucl. Mater., 119 (1983) 1-25.
[11] R.E. Stoller, G.R. Odette, J. Nucl. Mater., 131 (1985) 118-125.
[12] G.R. Odette, D.T. Hoelzer, Jom, 62 (2010) 84-92.
[13] L.K. Mansur, E.H. Lee, P.J. Maziasz, A.P. Rowcliffe, J. Nucl. Mater., 141-143 (1986) 633-646.
[14] G.R. Odette, R.E. Stoller, J. Nucl. Mater., 122 (1984) 514-519.
[15] G.R. Odette, M.J. Alinger, B.D. Wirth, Ann. Rev. Mater. Res., 38 (2008) 471-503.
[16] I.S. Kim, J.D. Hunn, N. Hashimoto, D.L. Larson, P.J. Maziasz, K. Miyahara, E.H. Lee, J. Nucl. Mater., 280 (2000) 264-274.
[17] D. Bhattacharyya, P. Dickerson, G.R. Odette, S.A. Maloy, A. Misra, M. Nastasi, Philos. Mag., submitted (2011).
[18] A.P. Sutton, R.W. Balluffi, Interfaces in Crystalline Materials, Oxford University Press, Oxford, 1995.
[19] P.L. Lane, P.J. Goodhew, Philos. Mag. A-Phys. Condens. Matter Struct. Defect Mech. Prop., 48 (1983) 965-986.
[20] B.N. Singh, T. Leffers, W.V. Green, M. Victoria, J. Nucl. Mater., 125 (1984) 287-297.
[21] P.A. Thorsen, J.B. Bilde-Sorensen, B.N. Singh, Scr. Mater., 51 (2004) 557-560.
[22] P.A. Thorsen, J.B. Bilde-Sorensen, B.N. Singh, Materials Science Forum, 207/209 (1996) 445-448.
[23] R.J. Kurtz, H.L. Heinisch, J. Nucl. Mater., 329 (2004) 1199-1203.
[24] J.X. Xia, W.Y. Hu, J.Y. Yang, B.Y. Ao, X.L. Wang, Phys. Status Solidi B-Basic Solid State Phys., 243 (2006) 2702-2710.
[25] F. Gao, H.L. Heinisch, R.J. Kurtz, J. Nucl. Mater., 367 (2007) 446-450.
[26] F. Gao, H. Heinisch, R.J. Kurtz, J. Nucl. Mater., 351 (2006) 133-140.
[27] A. Misra, J.P. Hirth, R.G. Hoagland, Acta Mater., 53 (2005) 4817-4824.
[28] B.N. Singh, Philos. Mag., 29 (1974) 25-42.
[29] M.J. Demkowicz, R.G. Hoagland, J.P. Hirth, Phys. Rev. Lett., 100 (2008) 136102.
[30] X.M. Bai, A.F. Voter, R.G. Hoagland, M. Nastasi, B.P. Uberuaga, Science, 327 (2010) 1631-1634.
[31] N. Li, M.S. Martin, O. Anderoglu, A. Misra, L. Shao, H. Wang, X. Zhang, Journal of Applied Physics, 105 (2009) 123522.
[32] N. Li, E.G. Fu, H. Wang, J.J. Carter, L. Shao, S.A. Maloy, A. Misra, X. Zhang, J. Nucl. Mater., 389 (2008) 233-238.
[33] J. Laakmann, P. Jung, W. Uelhoff, Acta Metallurgica, 35 (1987) 2063-2069.
[34] X. Zhang, N. Li, O. Anderoglu, H. Wang, J.G. Swadener, T. Hochbauer, A. Misra, R.G. Hoagland, Nuclear Instruments and Methods in Physics Research, Section B: Beam Interactions with Materials and Atoms, 261 (2007) 1129-1132.
[35] T. Hochbauer, A. Misra, K. Hattar, R.G. Hoagland, Journal of Applied Physics, 98 (2005) 123516-123511.

[36] D. Bhattacharyya, M.J. Demkowicz, Y.-Q. Wang, M. Nastasi, A. Misra, Microscopy and Microanalysis, submittted (2011).
[37] M. Zhernenkov, M.S. Jablin, A. Misra, M. Nastasi, Y.-Q. Wang, M.J. Demkowicz, J.K. Baldwin, J. Majewski, Applied Physics Letters, 98 (2011) 241913.
[38] M.J. Demkowicz, D. Bhattacharyya, I. Usov, Y.Q. Wang, M. Nastasi, A. Misra, Applied Physics Letters, 97 (2010).
[39] J.F. Ziegler, J.P. Biersack, U. Littmark, The Stopping and Range of Ions in Solids, Pergamon, New York, 1985.
[40] E.G. Fu, A. Misra, H. Wang, L. Shao, X. Zhang, J. Nucl. Mater., 407 (2010) 178-188.
[41] A. Kashinath, M.J. Demkowicz, Model. Simul. Mater. Sci. Eng., 19 (2011).
[42] T.E. Mitchell, Y.C. Lu, A.J. Griffin, M. Nastasi, H. Kung, J. Am. Ceram. Soc., 80 (1997) 1673-1676.
[43] X. Zhang, E.G. Fu, A. Misra, M.J. Demkowicz, Jom, 62 (2010) 75-78.
[44] M.J. Demkowicz, R.G. Hoagland, J. Nucl. Mater., 372 (2008) 45-52.
[45] M.J. Demkowicz, R.G. Hoagland, International Journal of Applied Mechanics, 1 (2009) 421.
[46] P.G. Shewmon, Diffusion in Solids, 2nd ed., Minerals, Metals & Materials Society, Warrendale, Pa., 1989.
[47] W. Bollmann, Crystal defects and crystalline interfaces, Springer-Verlag, Berlin, 1970.
[48] N. Li, J.J. Carter, A. Misra, L. Shao, H. Wang, X. Zhang, Philos. Mag. Lett., 91 (2010) 19-29.
[49] M.J. Demkowicz, O. Anderoglu, X. Zhang, A. Misra, J. Mater. Res., 26 (2011) 1666.
[50] Q.M. Wei, A. Misra, Acta Mater., 58 (2010) 4871-4882.
[51] J.P. Hirth, Journal of the Physics and Chemistry of Solids, 55 (1994) 985-989.
[52] Q.M. Wei, Y.Q. Wang, M. Nastasi, A. Misra, Philos. Mag., 91 (2011) 553-573.
[53] N. Li, N.A. Mara, Y.Q. Wang, M. Nastasi, A. Misra, Scr. Mater., 64 (2011) 974-977.
[54] A. Misra, M.J. Demkowicz, X. Zhang, R.G. Hoagland, Jom, 59 (2007) 62-65.
[55] U.F. Kocks, Materials Science and Engineering, 27 (1977) 291-298.
[56] J. Friedel, Dislocations, [1st English ed., Pergamon Press; U.S.A. ed. distributed by Addison-Wesley Pub. Co., Reading, Oxford, New York,, 1964.
[57] R.L. Fleischer, Acta Metallurgica, 10 (1962) 835.
[58] D.J. Bacon, U.F. Kocks, Scatterg.Ro, Philos. Mag., 28 (1973) 1241-1263.
[59] Y.N. Osetsky, D.J. Bacon, Philos. Mag., 90 (2010) 945-961.
[60] Q.Z. Li, P.M. Anderson, Acta Mater., 53 (2005) 1121-1134.
[61] A. Misra, R.G. Hoagland, J. Mater. Res., 20 (2005) 2046-2054.
[62] S.M. Han, M.A. Phillips, W.D. Nix, Acta Mater., 57 (2009) 4473-4490.
[63] M.A. Phillips, B.M. Clemens, W.D. Nix, Acta Mater., 51 (2003) 3157-3170.
[64] N. Li, R.G. Hoagland, J.P. Hirth, M. Nastasi, A. Misra, Acta Mater., submitted (2011).
[65] Q.M. Wei, N. Li, N.A. Mara, M. Nastasi, A. Misra, Acta Mater., in press (2011).
[66] R.G. Hoagland, J.P. Hirth, A. Misra, Philos. Mag., 86 (2006) 3537-3558.
[67] H. Trinkaus, Radiat. Eff. Defects Solids, 78 (1983) 189-211.
[68] S.Y. Hu, C.H. Henager, H.L. Heinisch, M. Stan, M.I. Baskes, S.M. Valone, J. Nucl. Mater., 392 (2009) 292-300.
[69] K. Morishita, R. Sugano, J. Nucl. Mater., 353 (2006) 52-65.

[70] I.R. Brearley, D.A. Macinnes, J. Nucl. Mater., 95 (1980) 239-252.
[71] R.L. Mills, D.H. Liebenberg, J.C. Bronson, Phys. Rev. B, 21 (1980) 5137-5148.
[72] A. Caro, J. Hetherly, A. Stukowski, M. Caro, E. Martinez, S. Srivilliputhur, L. Zapeda-Ruiz, M. Nastasi, J. Nucl. Mater., in press (2011).
[73] S.M.H. Haghighat, R. Schaublin, Philos. Mag., 90 (2010) 1075-1100.
[74] S.M.H. Haghighat, G. Lucas, R. Schaublin, Epl, 85 (2009).
[75] D.M. Stewart, Y.N. Osetsky, R.E. Stoller, S.I. Golubov, T. Seletskaia, P.J. Kamenski, Philos. Mag., 90 (2010) 935-944.
[76] N. Gao, M. Victoria, J. Chen, H. Van Swygenhoven, J. Phys.-Condes. Matter, 23 (2011) 245403.
[77] J. Hetherly, E. Martinez, A. Caro, M. Nastasi, J. Nucl. Mater., in press (2011).
[78] J. Hetherly, E. Martinez, Z.F. Di, M. Nastasi, A. Caro, Scr. Mater., submitted (2011).
[79] Z. Di, X.M. Bai, Q. Wei, J. Won, R.G. Hoagland, Y. Wang, A. Misra, B.P. Uberuaga, M. Nastasi, Phys. Rev. B, in press (2011).
[80] M.J. Demkowicz, Y.Q. Wang, R.G. Hoagland, O. Anderoglu, Nuclear Instruments and Methods in Physics Research, Section B: Beam Interactions with Materials and Atoms, 261 (2007) 524-528.
[81] K. Hattar, M.J. Demkowicz, A. Misra, I.M. Robertson, R.G. Hoagland, Scr. Mater., 58 (2008) 541-544.
[82] I.M. Robertson, C.A. Schuh, J. Vetrano, N.D. Browning, D. Field, D. Juul-Jensen, M. Miller, I. Baker, D.C. Dunand, R. Dunin-Borkowski, B. Kabius, T. Kelly, S. Lozano-Perez, A. Misra, G.S. Rohrer, A.D. Rollett, M. Taheri, G.B. Thompson, M. Uchic, X.L. Wang, G. Was, J. Mater. Res., 26 (2011) 1341.
[83] M.J. Demkowicz, P. Bellon, B.D. Wirth, MRS Bull., 35 (2010) 992-998.
[84] A. Misra, L. Thilly, MRS Bull., 35 (2010) 965-976.

Figure 1
Click here to download high resolution image

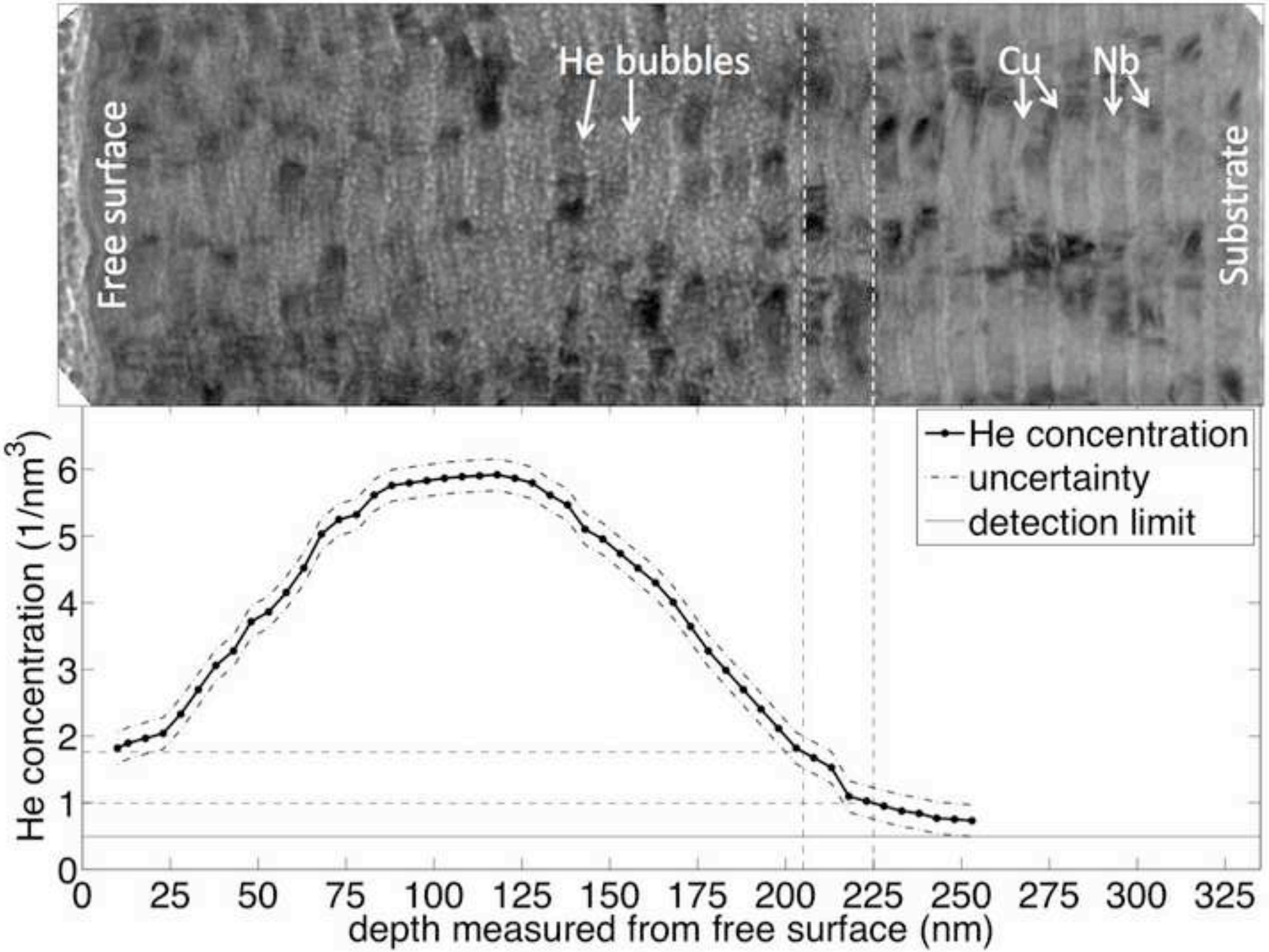

Figure 2
Click here to download high resolution image

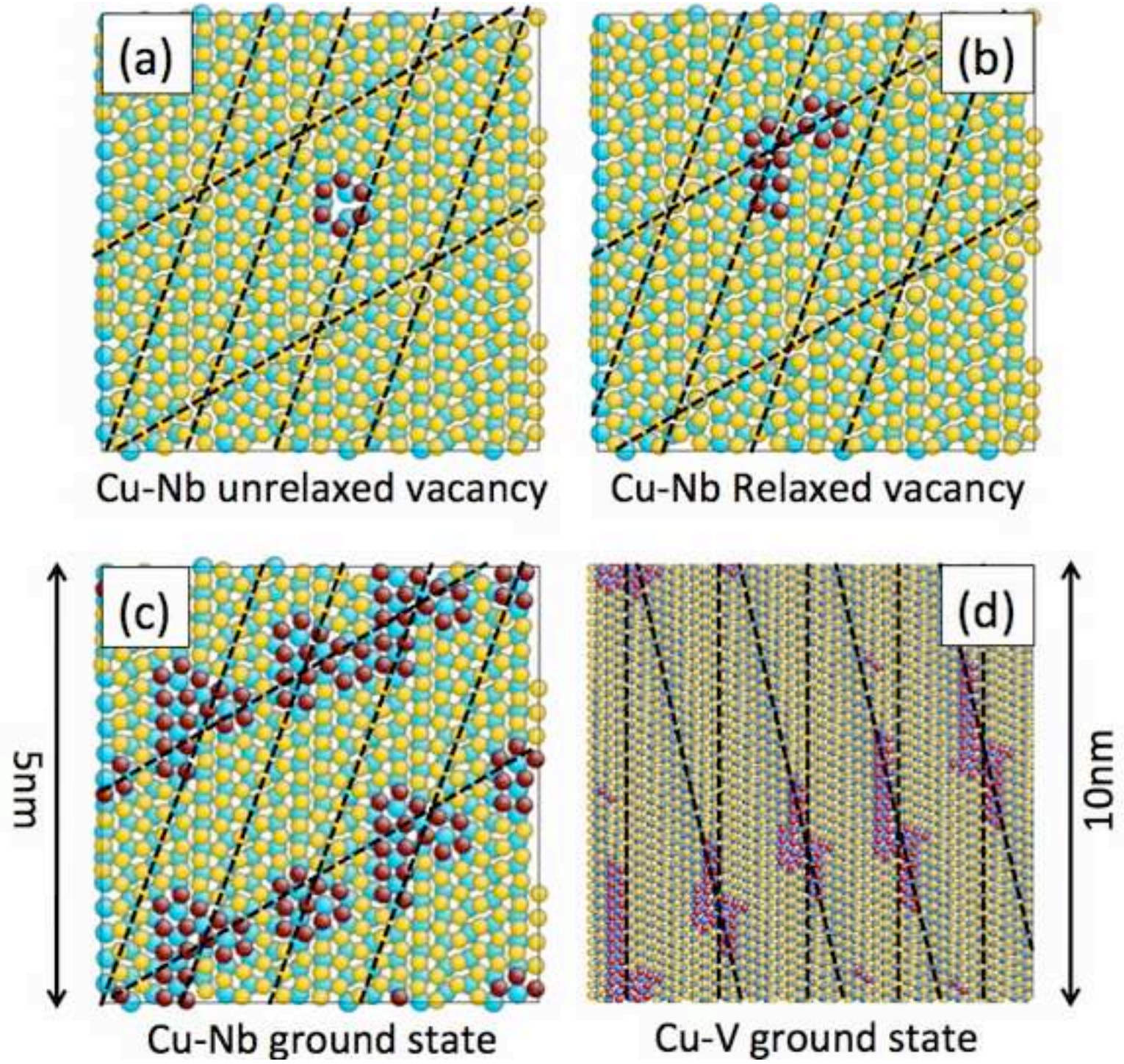

Figure 3

Click here to download high resolution image

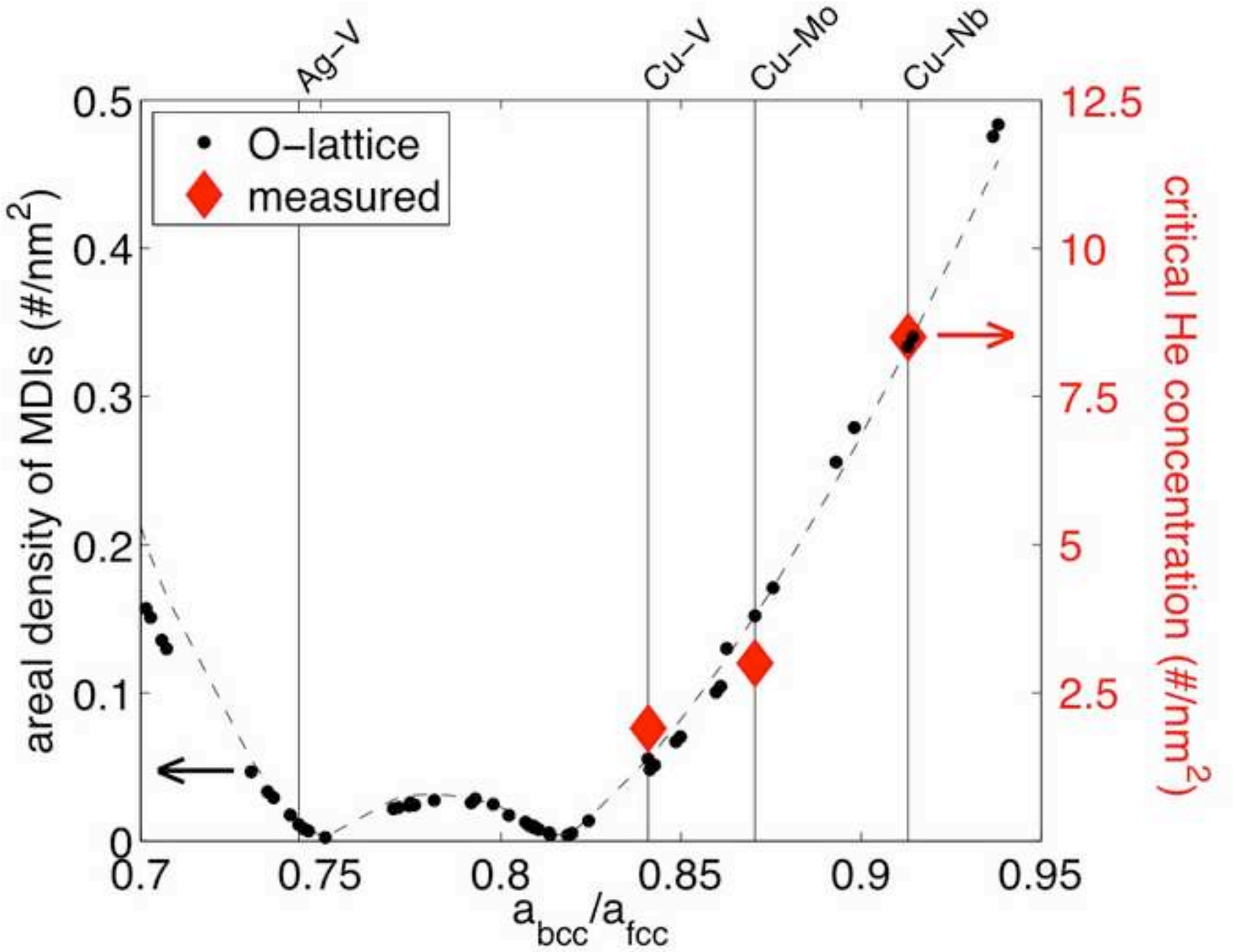

Figure 4

Click here to download high resolution image

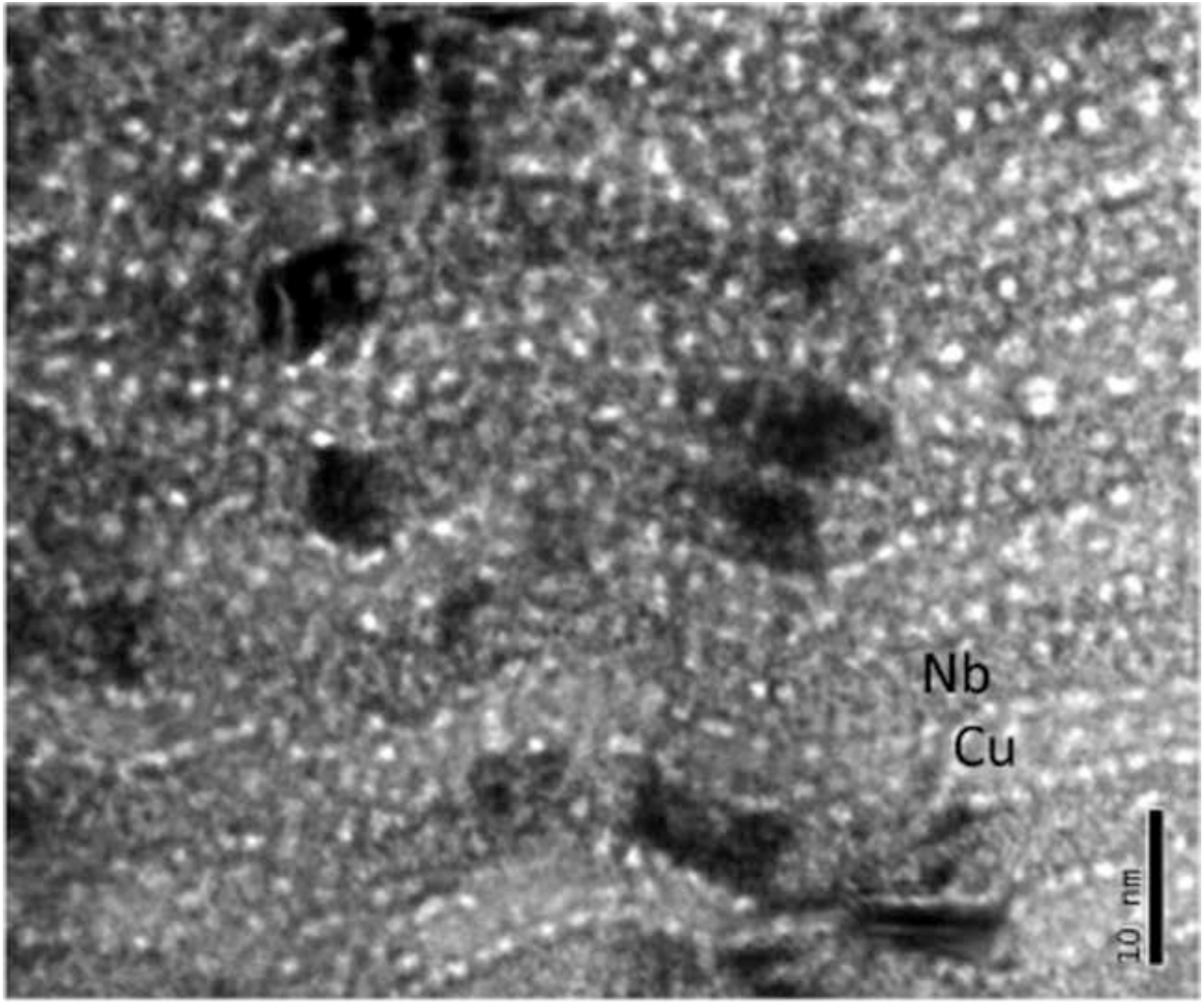

Figure 5
Click here to download high resolution image

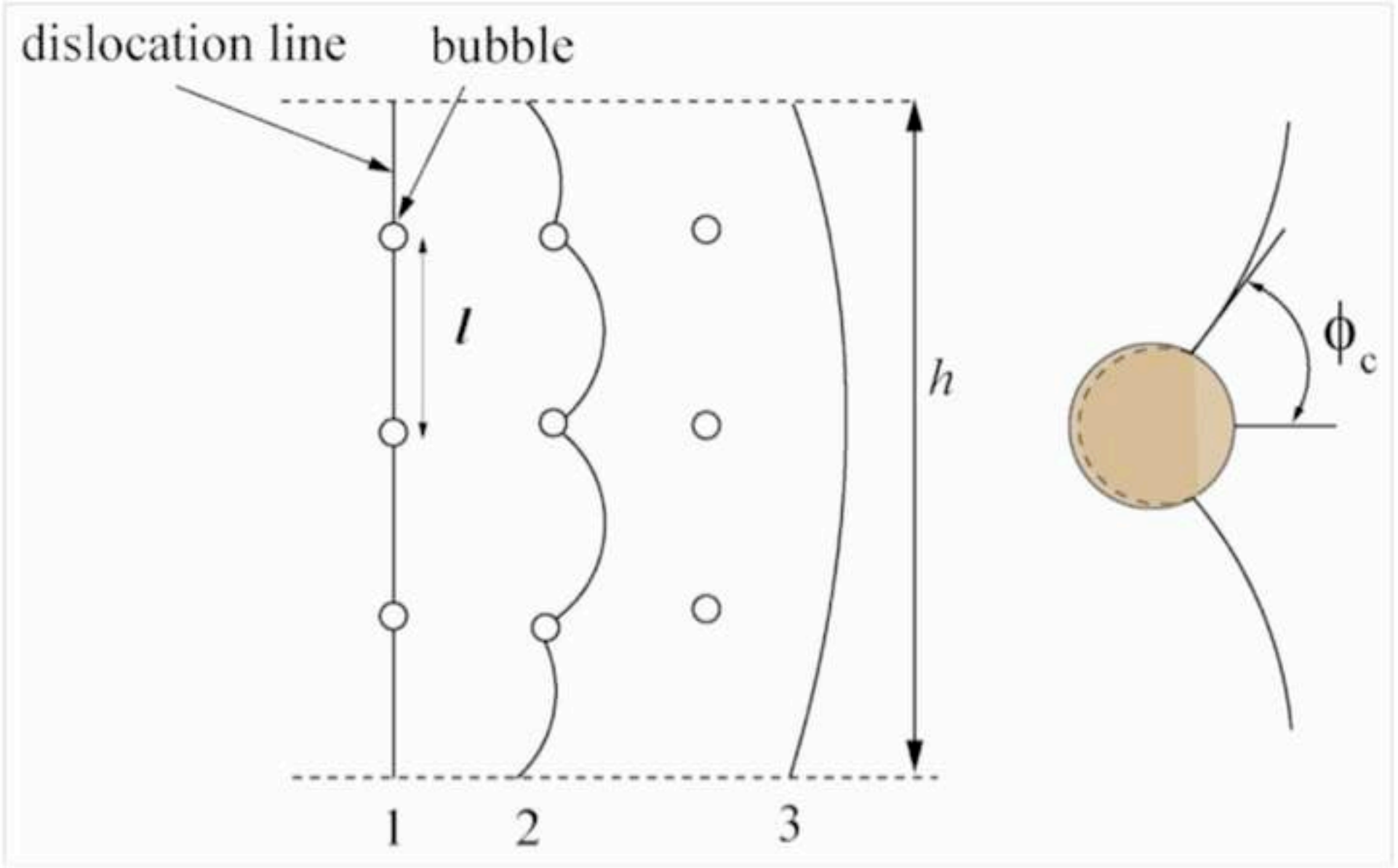

Figure 6

Click here to download high resolution image

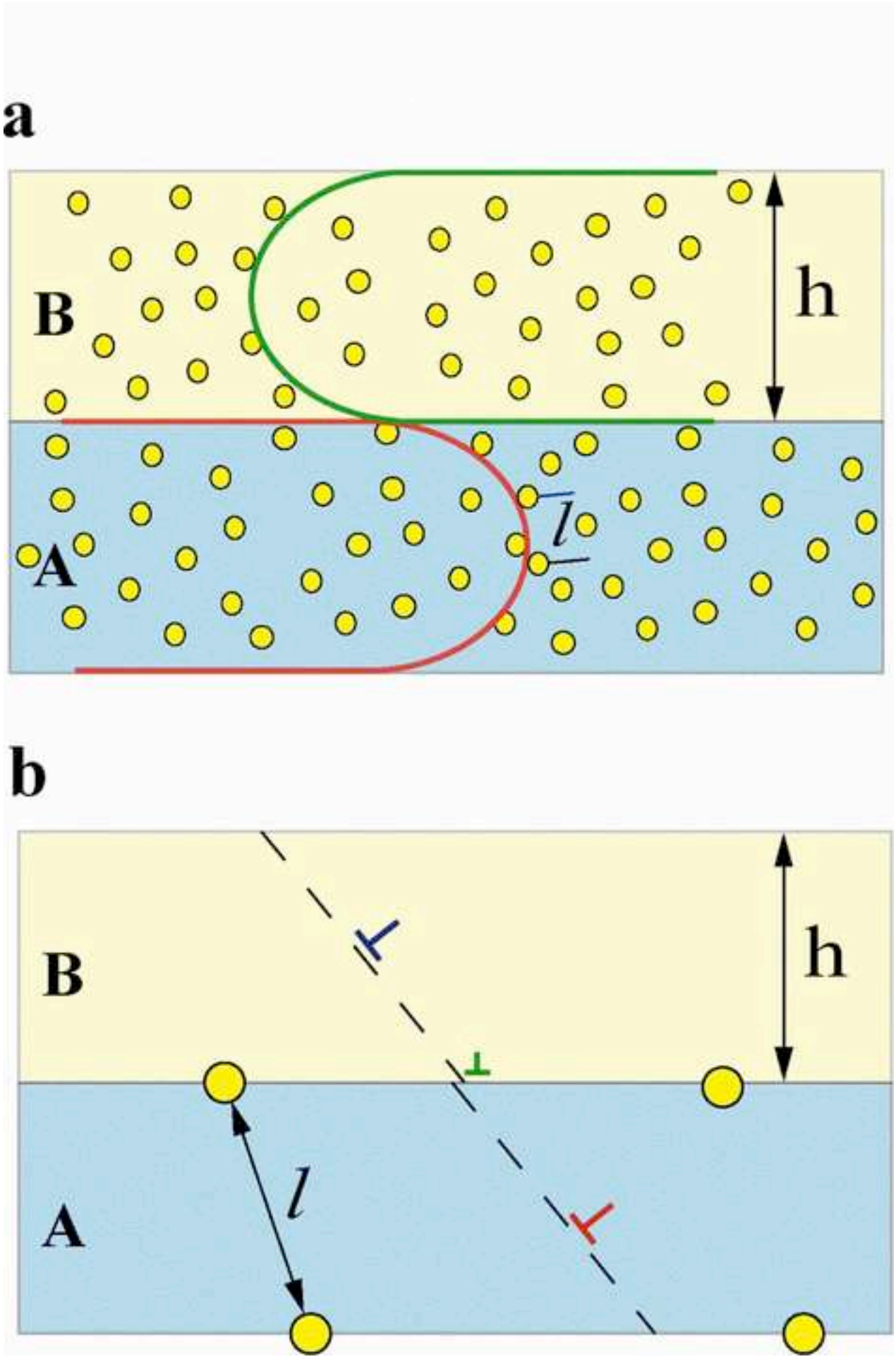

Figure 7

Click here to download high resolution image

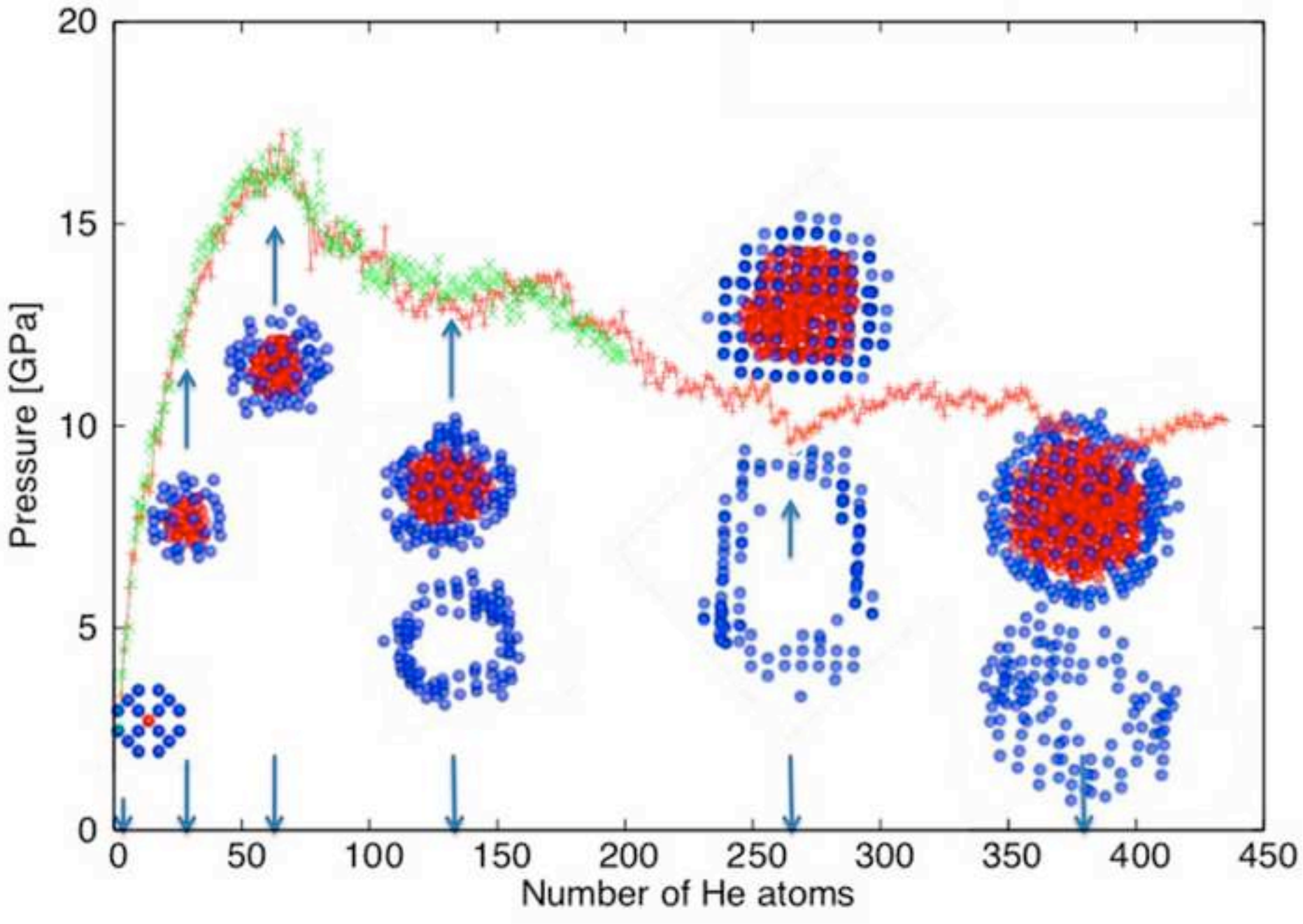

Figure 8
Click here to download high resolution image

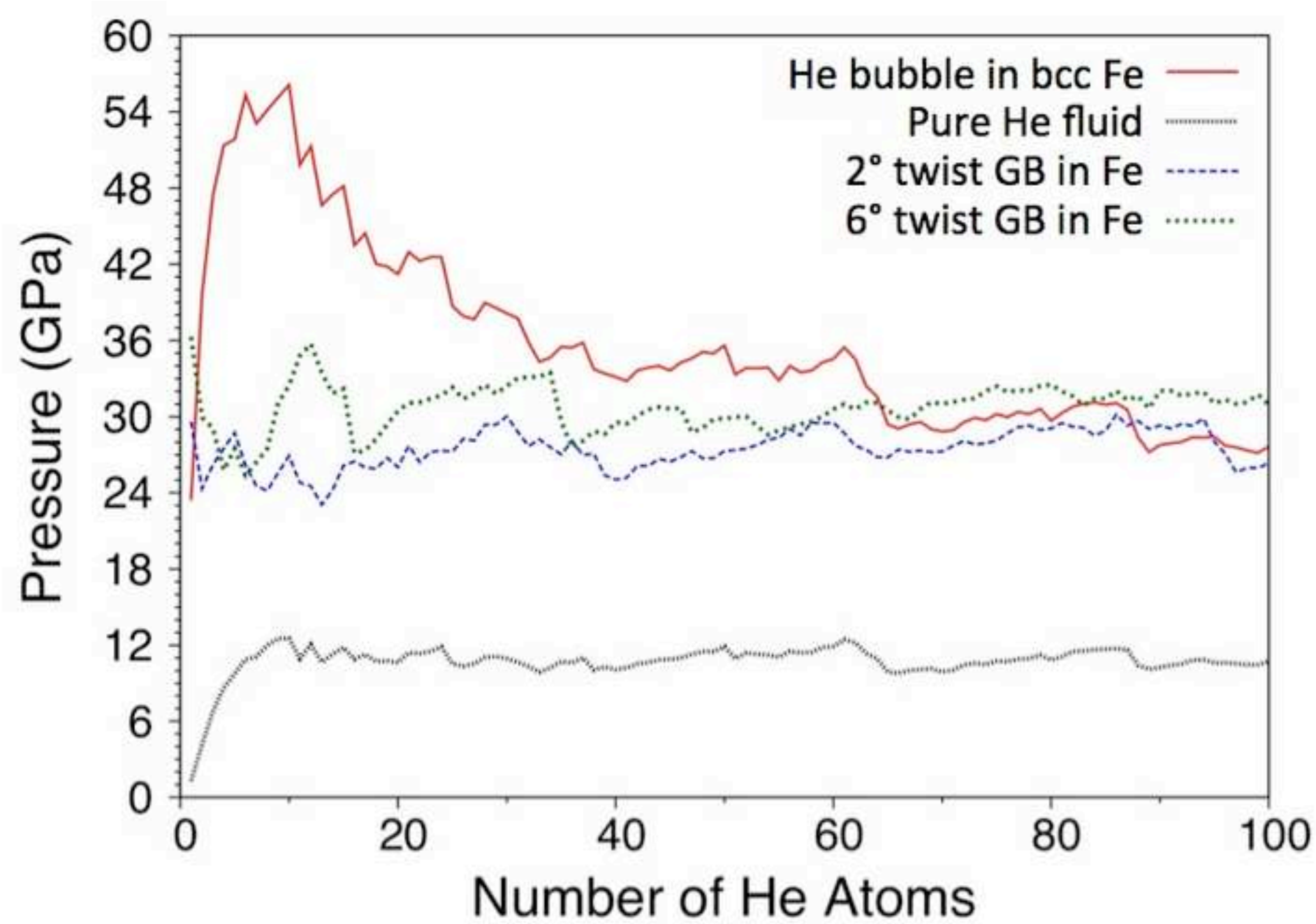

Figure 9

Click here to download high resolution image